Extreme Mechanics Letters 70 (2024) 102170



Contents lists available at ScienceDirect

Extreme Mechanics Letters

journal homepage: www.elsevier.com/locate/eml





A data-driven constitutive model for porous elastomers at large strains

M. Onur Bozkurt *, Vito L. Tagarielli *

Department of Aeronautics, Imperial College London, London SW7 2AZ, UK

ARTICLE INFO

Keywords:
Machine learning
Data-driven mechanics
Surrogate model
Porous elastomer
Computational homogenisation

ABSTRACT

A data-driven computational framework is established to implement surrogate constitutive models for porous elastomers undergoing large deformation. Explicit finite element (FE) simulations are conducted to compute the homogenised response of a cubic unit cell of a porous compressible elastomer, subject to a random set of imposed multiaxial strain states. The FE predictions are used to assemble a training dataset for two different surrogate models, based on simple neural networks. The first establishes a non-linear correspondence between six-dimensional strain and stress vectors; the second provides a strain energy potential from which to derive the stress versus strain response. The accuracy of the surrogate models is quantified, and their predictions are compared to those of the Hyperfoam model; it is found that the surrogate models can significantly outperform this well-known phenomenological model.

1. Introduction

Porous elastomers have received significant technological interest due to their versatile properties and wide-ranging applications. These lightweight materials are known by their remarkable ability to undergo large deformations and to absorb energy. With their distinct properties, porous elastomers are preferred for the purposes of vibration isolation [1], acoustic and thermal insulation [2,3], impact mitigation [4], and shock absorption [5] in vehicle and aerospace engineering. They are also increasingly being utilised in biomedical engineering as scaffold for tissue growth and drug delivery applications [6-8]. Furthermore, the high flexibility and low modulus of elastomers make them suitable for tactile sensors in soft robotics [9,10], and wearable devices such as pressure sensors [11] and energy harvesters [12] which require conformity to irregular surfaces. In these and many other practical situations, porous elastomers are subjected to significant deformations, making it important to develop constitutive models that accurately capture their mechanical behaviour under such loading conditions.

Theoretical attempts at non-linear elastic modelling of porous materials date back to Ogden's pioneering work [13], where the finite strain generalisations of the Voigt, Hill, and Reuss estimates of the moduli were derived under isochoric deformations. Hashin [14] presented an exact solution for large isotropic compression and expansion of porous materials based on a composite spheres assemblage model. Danielsson et al. [15] developed a general expression for the strain energy density function for porous materials with an incompressible hyperelastic matrix material, which was achieved by solving the kinematically admissible deformation field for the cavity growth in a solid based on the incompressibility assumption. More recently, Shrimali et al. [16] proposed an approximate homogenisation solution for explicit formulation of the strain energy function for porous materials with an incompressible matrix. These models can predict hyperelastic mechanical response with substantial accuracy; however, they have several drawbacks such as their limitation to incompressible matrix materials and their inability to capture pre-densification response at large compressive deformation as they do not account for local buckling instabilities [17].

The limitations of theoretical approaches have heightened interest in the development of phenomenological constitutive models that rely on fitting experimental stress-strain data of porous elastomers. Storåkers [18] showed that an Ogden-type principal stretch-based strain energy density function can reproduce the homogenous hyperelastic response of porous elastomers. Landauer et al. [17] proposed a strain energy density function depending on the invariants of the logarithmic strain tensor, with special focus on modelling the large deformation response of open cell elastomeric foams. While these models are capable of predicting the hyperelastic response of porous elastomers, they may pose practical challenges and incur costs, as they require experimental characterization of the material parameters for a range of porosity levels through the application of multiple homogeneous deformation modes or a single tension/compression test with full-field strain measurement.

Due to the limitations and challenges associated with traditional

* Corresponding authors.
E-mail addresses: o.bozkurt20@imperial.ac.uk (M.O. Bozkurt), v.tagarielli@imperial.ac.uk (V.L. Tagarielli).

https://doi.org/10.1016/j.eml.2024.102170
Received 31 January 2024; Received in revised form 14 May 2024; Accepted 17 May 2024
Available online 21 May 2024
2352-4316/© 2024 The Author(s). Published by Elsevier Ltd. This is an open access article under the CC BY license (http://creativecommons.org/licenses/by/4.0/).

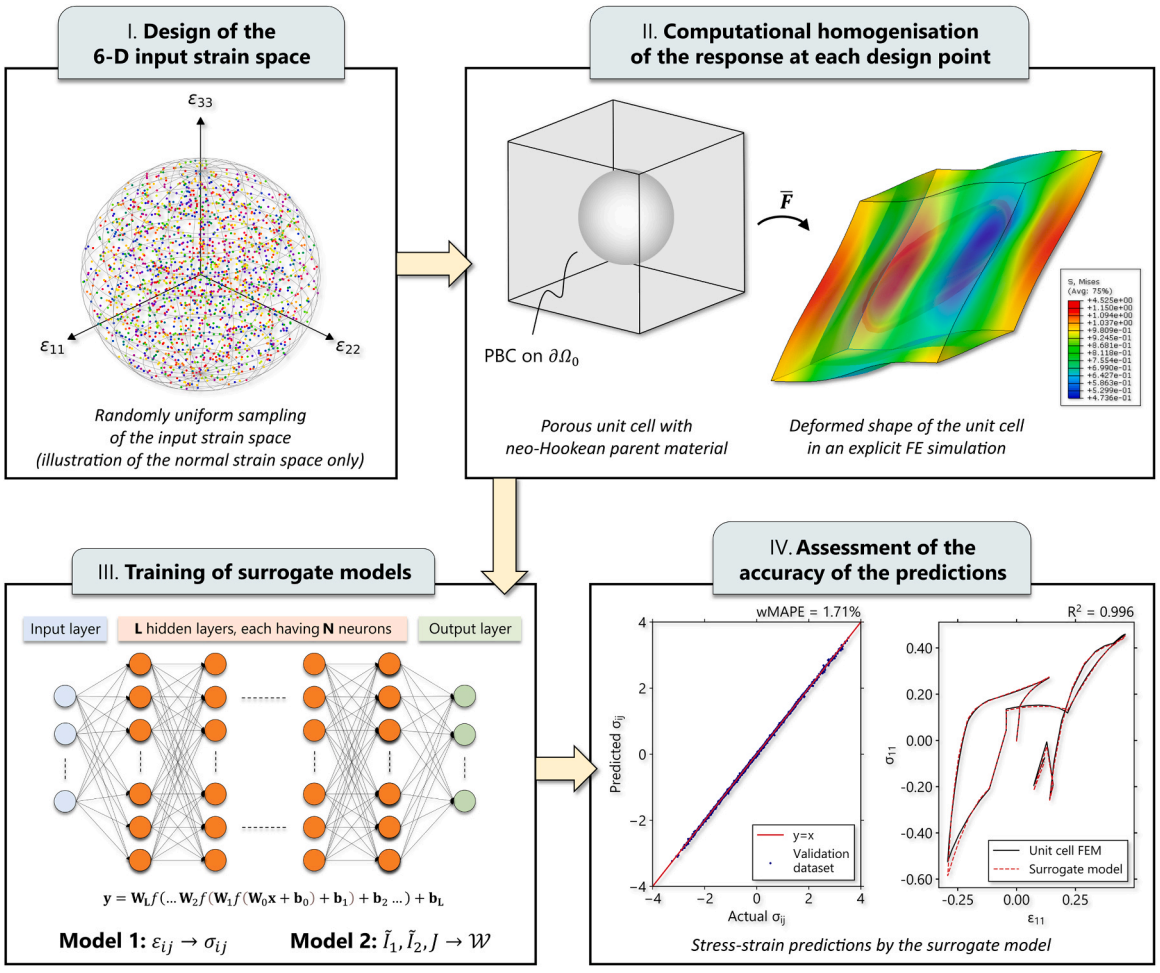


Fig. 1. Schematic representation of the proposed computational framework. I. A 6-dimensional set of points with randomly uniform distribution. II. Homogenisation of the response of a porous unit cell via explicit finite element simulations. III. Training of the two surrogate models. IV. Assessment of the accuracy of the predictions.

analytical and phenomenological approaches in constitutive modelling, computational homogenisation-based multiscale modelling of porous elastomers has received significant attention. Several researchers have employed computational homogenization to predict the finite deformation response of porous elastomers using various porous microstructures, such as a 2-D unit cell with a circular pore [19-21], a 2-D periodic representative volume element (RVE) with circular pores [22,23], a 3-D unit cell with a spherical pore [19,24], and a 3-D periodic RVE with spherical pores [25,26,16,27]. While these approaches yield precise and physically interpretable predictions, the computational cost associated with applying the micromechanical solution to structures of larger scales can often be prohibitive. This provides an opportunity to apply machine learning to the problem.

Data-driven surrogate constitutive models have been gaining popularity. Le et al. [28] demonstrated first that an effective potential for non-linear elastic composites can be predicted by a neural network (NN). Bessa et al. [29] presented a unifying approach for data-driven surrogate modelling of heterogenous materials by integrating design of experiments, computational analyses, and machine learning. Later, Mozaffar et al. [30] predicted path-dependent plasticity by means of recurrent neural networks (RNNs). Yang et al. [31] leveraged principal component analysis (PCA) and convolutional neural networks (CNNs) to predict the entire stress-strain behaviour of a composite based on the image of its microstructure. Ge and Tagarielli [32] proposed a computational framework for NN-based surrogate modelling of multiphase composites with hyperelastic, viscoelastic and elastic–plastic local constitutive descriptions. Building upon this previous work, Ge and Tagarielli [33] extended their framework to capture the progressive damage response of heterogeneous ductile solids. Logarzo et al. [34] proposed smart constitutive laws, which perform inelastic homogenisation through long short-term memory (LSTM) networks trained with strain-paths generated by Gaussian Processes (GP). More recently, Frankel et al. [35] reported a comparative study on the performance of feed-forward NNs (FFNNs) and Gaussian Processes Regression (GPR) in predicting principal stress vs strain behaviour of elastomeric foams. It is also noteworthy that several researchers employed experimental data-driven strategies to surrogate complex multiaxial experiments of elastic-plastic materials [36,37], to forecast the finite fatigue life of additively manufactured materials [38,39], and to calibrate hyperelastic constitutive models with full-field strain data [40]. Additional references on the application of machine learning in modelling the mechanical behaviour of materials can be found in the review article by Guo et al. [41].

There has also been a significant focus on preserving the basic principles of solid mechanics in machine learning-based constitutive models. To ensure objectivity and material symmetry, Ling et al. [42] used invariance property as input to their model and compared the predictive capabilities of NNs and random forest (RF) in a problem of crystal elasticity. Vlassis et al. [43] proposed a hybrid approach incorporating geometric deep learning and FFNNs to predict anisotropic hyperelasticity from connectivity of anisotropic grains. Although their model predicts the strain energy potential, they implemented a modified loss function which enables the optimisation of FFNNs to minimise error in stress predictions. Fernández et al. [44] compared the predictive

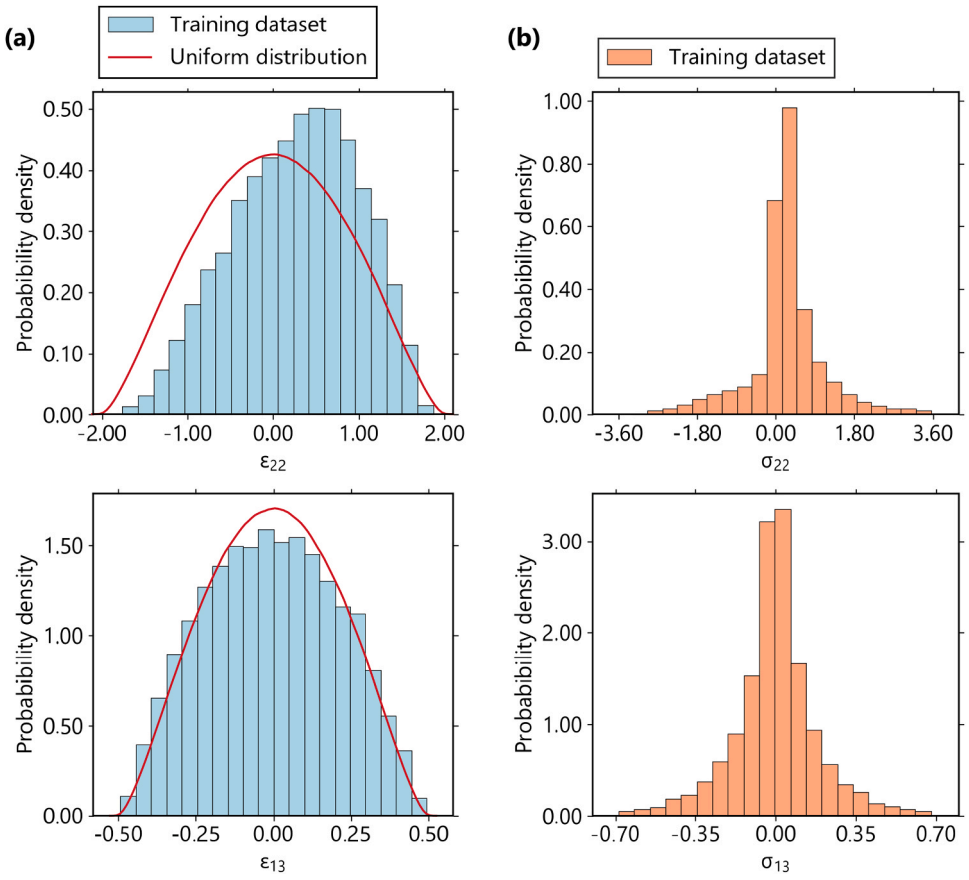


Fig. 2. Probability densities of (a) true strain and (b) true stress components in the training dataset. The 22 and 13 components are plotted. The curves in (a) correspond to the probability density expected for a uniform 6-D set of points.

capabilities of anisotropic hyperelastic and simple elastic NN-based formulations for cubic lattice metamaterials, trained by only canonical test data. Linka et al. [45], inspired from mathematical formulations of phenomenological hyperelastic constitutive laws, proposed the so-called constitutive artificial neural networks (ANNs) which can quantify the roles of different deformation modes and of their interaction on the mechanical response with separate sub-ANNs. Recently, As'ad et al. [46] demonstrated that enforcing mechanics-based constraints to NN predictor by modifying the architecture and the loss function not only improves the model to interpolate inside the training space, but also adds a decent level of extrapolation capability. For a comprehensive overview of recent advancements in data-driven constitutive laws for solids, readers are referred to the review article by Fuhg et al. [47].

In this study, we develop a NN-based data-driven surrogate model for predicting the finite strain behaviour of porous elastomers with a compressible neo-Hookean parent material. The objective is two-fold: to reduce the computational cost of multiscale analyses, and to develop adequate strategies to implement surrogate constitutive models informed directly by high-fidelity synthetic data. Fig. 1 summarises the computational framework presented, in 4 steps: (i) designing the training dataset to ensure that the input strain space is explored randomly uniformly, (ii) conducting a set of high-fidelity FE analyses of the response of a porous unit cell, obtaining output stress data as a function of the imposed deformation, (iii) training data-driven surrogate models relying on FFNNs, and (iv) testing the accuracy of the surrogate models. In the rest of the article, we will discuss these steps in detail.

2. Generation of data

2.1. Design of the training data space

We first aim at developing a surrogate model to establish a non-linear relation between the true (i.e. Hencky, logarithmic) strain $\boldsymbol{\varepsilon}$ and true (i.e. Cauchy) stress $\boldsymbol{\sigma}^*$. We operate on a non-dimensional version of the stress vector $\boldsymbol{\sigma} = \boldsymbol{\sigma}^*/E_0$, where E_0 is the initial Young's modulus of the isotropic matrix material. The constitutive response of the unit cell depends on the initial Poisson's ratio ν_0 of the neo-Hookean parent material and on the initial porosity p_0. In this study, we do not explore the effects of varying material properties (ν_0) or initial porosity but focus on capturing accurately the stress versus strain response for given initial values of ν_0 and p_0 (ν_0=0.45, p_0=0.1). Due to the symmetry of true strain and true stress tensors, we simply formulate a constitutive mapping between 6-D vector forms of their upper triangular matrices as $\boldsymbol{\sigma} = \mathscr{F}(\boldsymbol{\varepsilon})$, where $\mathscr{F}$: $\mathbb{R}^6 \rightarrow \mathbb{R}^6$, $\boldsymbol{\varepsilon} = \{\varepsilon_{11}, \varepsilon_{22}, \varepsilon_{33}, \varepsilon_{12}, \varepsilon_{13}, \varepsilon_{23}\}^T$, $\boldsymbol{\sigma} = \{\sigma_{11}, \sigma_{22}, \sigma_{33}, \sigma_{12}, \sigma_{13}, \sigma_{23}\}^T$.

A common strategy for implementing surrogate models is to achieve an effective coverage of the input space [48]. For this purpose, we sample 27,000 design points, randomly uniform in a unit 6-ball using the method of dropped coordinates [49]. This imaginary unit 6-ball is then transformed into the 6-D cloud of true strain vectors by stretching it to the extreme strain values in each of the 6 principal dimensions. Without loss of generality, we assume $\varepsilon_{ii} \in$ [-2,2] and $\varepsilon_{ij} \in$ [-0.5,0.5] where $i, j = 1, 2, 3$, implying that the actual input space is a hyper-ellipsoid in $\mathbb{R}^6$.

Fig. 2a illustrates the probability distributions (PD) of normal and shear components of true strain (a) and true stress (b), in conjunction with the comparison of achieved strain distribution to the theoretical uniform distribution in $\mathbb{R}^6$. The distribution of the shear strain

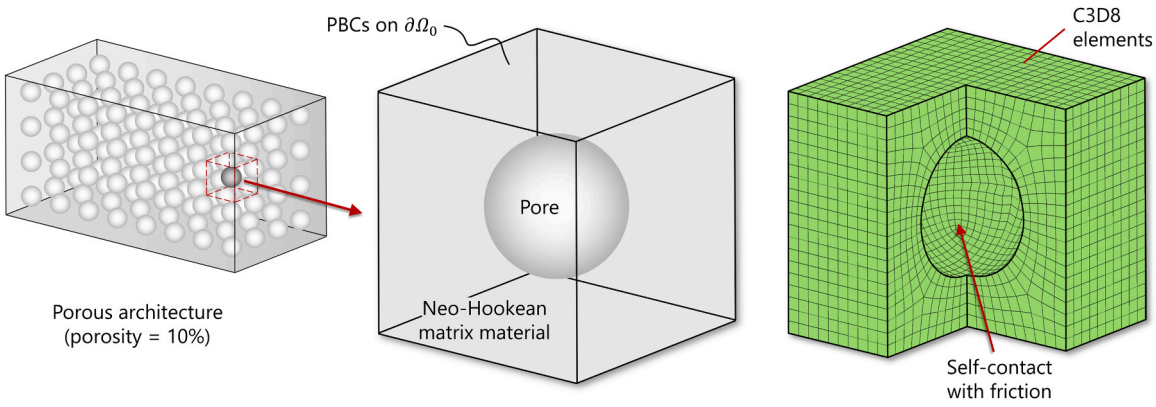


Fig. 3. Representative porous unit-cell structure and its discretization in ABAQUS/Explicit.

component ε_{13} is close to the expected one, while that of the normal strain ε_{22} is slightly skewed to the right. This imperfection is due to a large number of FE analyses that did not complete as planned, in particular these were becoming unstable at large compressive strains. The disparities in the PD shapes of the corresponding strain and stress components are a consequence of the nonlinear elastic response exhibited by the porous unit cell.

2.2. Finite element analyses

In this study we use ABAQUS/Explicit 2022 to analyse the homogenised response of an elastomer of 10% porosity, assumed to have a periodic structure with simple cubic symmetry, as illustrated in Fig. 3. The model cannot compute the interaction between adjacent pores, it is therefore adequate for small porosity, hence our choice of 10%. The cubic packing is known to predict a response very similar to that of random arrays of pores [19,50]. We opt for a periodic structure to minimise the computational cost of the investigation. The edge of the unit cell is taken 1 mm in length without loss of generality. Geometrical non-linearity was taken into account in all FE analyses.

The parent material of the porous elastomer is described by the compressible neo-Hookean hyperelastic formulation, corresponding to a strain energy density [51]

$$\mathscr{W} = \frac{\mu_0}{2}(\widetilde{I}_1 - 3) + \frac{K_0}{2}(J-1)^2 \tag{1}$$

where μ_0 and K_0 are material properties, $\widetilde{I}_1$ is the first invariant of the isochoric left Cauchy-Green deformation tensor $\widetilde{\boldsymbol{B}}$, and J is the Jacobian determinant of the deformation gradient tensor, $\boldsymbol{F}$. μ_0 and K_0 are the initial shear and bulk moduli of the solid material, respectively, and they can be expressed as $\mu_0 = E_0/2(1+\nu_0)$ and $K_0 = E_0/3(1-2\nu_0)$. The initial Poisson's ratio of the isotropic parent material, ν_0, was taken as 0.45.

The porous unit cell is meshed with a structured mesh of 8-noded, fully integrated, 3-dimensional hexahedral elements (C3D8 in ABAQUS/Explicit) as shown in Fig. 3. Following a mesh convergence study (see Appendix I), each edge of the cubic geometry is discretised with 20 elements. Hertzian contact with a friction coefficient of 1 was defined via the general contact algorithm, to capture the behaviour of the unit cell at large compressive strains. The choice of the friction coefficient of 1 is arbitrary within the approximate range reported for rubbers on dry surfaces [51]. The choice of frictional versus frictionless contact followed from a preliminary study that showed that frictionless contact let to spurious local dynamic responses, due to the relative tangential slipping of the two surfaces in contact. The study also revealed that the recorded macroscopic stress versus strain response was not insensitive to the chosen value of the coefficient of friction. However, the amount of the frictional dissipation at the pore contact was found insignificant compared to the internal energy, such that the unit cell modelled has practically a conservative and path-independent mechanical response.

In analysing large compressive deformation response of porous materials by means of implicit FE solutions, convergence issues, which result in incomplete simulations, are often spotted [16]. In our preliminary implicit runs, we identified the lack of positive definiteness of the system matrix as the reason for non-convergence. Although, this can be associated with physical problems such as a compressive load surpassing the bifurcation point or a material instability often due to large strains, it could also be a numerical artifact resulting from excessive distortion of finite elements or the limited mesh quality near the pore. The proposed solution to bypass this difficulty is to perform an explicit solution during which the formulation of the tangent stiffness matrix is not derived [52]. Therefore, Abaqus/Explicit was preferred to standard due to its greater stability in non-linear analyses. It is worth noting that this choice implies that the generated data and thus the constitutive model to be trained do not account for local buckling phenomena that may occur under large compressive deformations.

The robustness of these explicit simulations, using carefully selected parameters, has been demonstrated by their ability to accurately predict the identical stress-strain response as the reference implicit FE model in numerous test cases. Reasonable computation times were achieved in Explicit by applying mass scaling and increasing the rate of deformation with the application of boundary displacements via smooth-step amplitudes, while checking that the kinetic energy in the models was $\ll$1% of the internal energy of the system, in all simulations. The detailed procedure for determining the explicit simulation parameters is reported in Appendix II.

16,429 simulations were completed, corresponding to an equal number of 6-D states of true strain and true stress. A single analysis took approximately 35 mins on average on a single core of an AMD EPYC 7742 server CPU.

The training dataset was constructed based on the homogenised deformation gradient, 1st Piola-Kirchhoff stress, strain energy density at target values of $\boldsymbol{\varepsilon}$. Other stress and deformation measures were obtained from these quantities by means of well-established analytical relations. ~8% of the data points collected from the simulations were classified as outliers and removed from the dataset.

2.3. Computational homogenisation

The unit cell Ω of a porous periodic microstructure had boundary denoted by $\partial\Omega$. The local-global equivalence of the constitutive response is verified by satisfaction of the Hill-Mandel condition (also known as the macrohomogeneity condition), which reads as:

$$\langle \boldsymbol{P}\cdot\boldsymbol{F}\rangle = \langle \boldsymbol{P}\rangle\langle \boldsymbol{F}\rangle \tag{2}$$

where $\langle\bullet\rangle$ indicates the volume average over the domain Ω, $\boldsymbol{P}$ denotes the microscopic (local) 1st Piola-Kirchhoff stress tensor, and $\boldsymbol{F}$ denotes

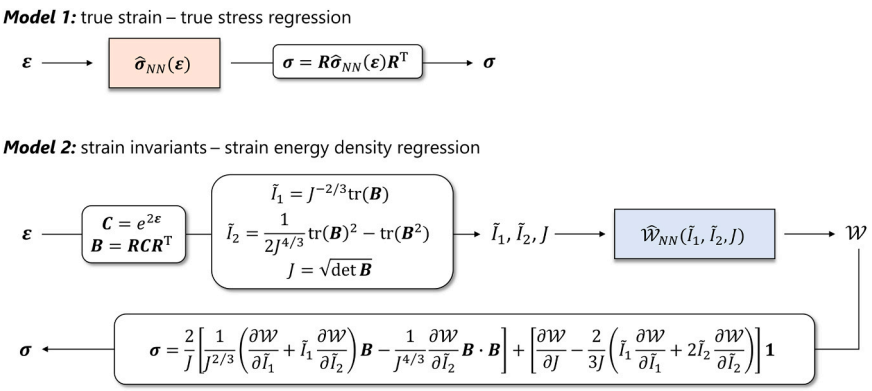


Fig. 4. Schematical illustration of the two surrogate models. In Model 1, a neural network establishes a direct relation between true strains and true stresses. In Model 2, a neural network is trained to predict the strain energy density potential as a function of the strain invariants, which is used to predict the stress.

the microscopic deformation gradient. The Hill-Mandel condition ensures the energetic consistency across the scales [53]. Using the Hill-Mandel condition in conjunction with the average strain theorem, under quasi-static conditions and in the absence of body forces, the macroscopic deformation gradient $\overline{\boldsymbol{F}}$ can be defined as:

$$\overline{\boldsymbol{F}} = \langle \boldsymbol{F} \rangle \tag{3}$$

Similarly, using the Hill-Mandel condition in conjunction with the average stress theorem, the macroscopic 1st Piola-Kirchhoff stress tensor $\overline{\boldsymbol{P}}$ can be defined, under quasi-static conditions and in the absence of body forces, as:

$$\bar{\boldsymbol{P}} = \langle \boldsymbol{P} \rangle. \tag{4}$$

Periodic boundary conditions are chosen due to the well-known advantages over other types of boundary conditions [54]. They read:

$$\boldsymbol{x}^{+} - \boldsymbol{x}^{-} = \bar{\boldsymbol{F}}\,(\boldsymbol{X}^{+} - \boldsymbol{X}^{-}) \text{ and } \boldsymbol{T}^{+} = -\boldsymbol{T}^{-} \text{ on } \partial\Omega \tag{5}$$

where $\boldsymbol{X}$, $\boldsymbol{x}$, and $\boldsymbol{T}$ denote the undeformed coordinates, deformed coordinates, and tractions, respectively. Superscripts + and – indicate the vectors on two counterparts $\partial\Omega^{+}$ and $\partial\Omega^{-}$ of the boundary $\partial\Omega$, through which the periodicity is imposed. The former equality in Eq. (5) imposes periodic displacements and the latter imposes anti-periodic tractions. If the unit cell is in equilibrium, the anti-periodicity of tractions is ensured a priori by the anti-periodicity of the surface normal vectors, i.e., $\boldsymbol{N}^{-} = -\boldsymbol{N}^{+}$ on $\partial\Omega$.

Using the definition of displacement vector $\boldsymbol{u} = \boldsymbol{X} - \boldsymbol{x}$, we can rewrite the first equality in Eq. (5) as:

$$\boldsymbol{u}^{+} - \boldsymbol{u}^{-} = \left(\bar{\boldsymbol{F}} - \boldsymbol{I}\right)(\boldsymbol{X}^{+} - \boldsymbol{X}^{-}) \text{ on } \partial\Omega, \tag{6}$$

or in indicial notation for the cubic unit cell as

$$u_i^{k+} - u_i^{k-} = \left(\bar{F}_{ij} - \delta_{ij}\right)\left(X_j^{k+} - X_j^{k-}\right) \text{ on } \partial\Omega \tag{7}$$

where superscripts $k+$ and $k-$ denotes the two opposing surfaces of the unit cell with a normal directed in the k^{th} coordinate axis, and δ_{ij} is the Kronecker's delta.

In the non-dimensional framework, where the characteristic length of the model is the edge length of the simple cubic unit cell, the non-dimensional quantity $X_j^{k+} - X_j^{k-}$ equals 1 if $k = j$, equals 0 otherwise. Therefore, in the non-dimensional framework, PBCs for the simple cubic unit cell reduces to:

$$u_i^{j+} - u_i^{j-} = \bar{F}_{ij} - \delta_{ij} \tag{8}$$

where the right-hand side of Eq. (8) is equivalent to the macroscopic displacement gradient. A practical and efficient approach for implementing PBCs to the FE model is creating 3 reference points (RP) each having 3 degrees of freedoms (DOF), at which 9 components of the macroscopic displacement gradient are prescribed as displacements [55], as:

$$u_i^{RP-j} = \bar{F}_{ij} - \delta_{ij} \tag{9}$$

where $u_i^{RP\text{-}j}$ is the displacement of the i$^{\text{th}}$ DOF of the k$^{\text{th}}$ RP. Combining Eqs. (8) and (9), the general form of the constraint equations used to formulate PBCs across the opposing surface, edge, and corner nodes of the cubic unit cell is obtained as:

$$u_i^{j+} - u_i^{j-} = u_i^{RP-j}. \tag{10}$$

Some of the constraints across the edges and vertices are redundant and the implementation of the above set of equations to the FE model should be carried out with extreme attention to avoid over-constraining the unit cell [56]. Explicit forms of the constraint equations are listed in the Appendix III.

If the unit cell is in equilibrium, the non-dimensional macroscopic 1st Piola-Kirchhoff stresses (or equivalently nominal stresses by definition) is simply obtained as the reaction forces at the DOFs of the RPs as:

$$\bar{P}_{ij} = R_i^{RP-j}. \tag{11}$$

It is noted that only $\overline{\boldsymbol{F}}$ and $\overline{\boldsymbol{P}}$ can be obtained by volume averaging their microscopic counterparts over the domain Ω [21]. Other macroscopic deformation and stress measures should be obtained using $\overline{\boldsymbol{F}}$ and $\overline{\boldsymbol{P}}$ as:

$$\begin{aligned} \bar{J} &= \det \overline{\boldsymbol{F}} \neq \langle J \rangle \\ \bar{\boldsymbol{\varepsilon}} &= \frac{1}{2}\ln \overline{\boldsymbol{F}}^{\mathrm{T}}\,\overline{\boldsymbol{F}} \neq \langle \boldsymbol{\varepsilon} \rangle \\ \bar{\boldsymbol{\sigma}} &= \frac{1}{\bar{J}}\overline{\boldsymbol{F}}\,\overline{\boldsymbol{P}} \neq \langle \boldsymbol{\sigma} \rangle. \end{aligned} \tag{12}$$

The outlined approach requires prescribing 9 components of the macroscopic displacement gradient ($\overline{F}_{ij}$–δ_{ij}). Conversely, the training data space is designed to ensure a uniformly random distribution of the symmetric true strain matrix in $\mathbb{R}^6$. Therefore, for every design point, it is necessary to compute the deformation gradient $\overline{\boldsymbol{F}}$ from the true strain $\bar{\boldsymbol{\varepsilon}}$ through the right polar decomposition theorem,

$$\bar{\boldsymbol{F}} = \bar{\boldsymbol{R}}\,\bar{\boldsymbol{U}} = \bar{\boldsymbol{R}}\,e^{\bar{\boldsymbol{\varepsilon}}} \tag{13}$$

where $\overline{\boldsymbol{U}}$ and $\overline{\boldsymbol{R}}$ are the right stretch and finite rotation tensors, respectively. Eq. (13) demonstrates the fact that as many macroscopic FE simulations can be conducted for each design point as there are different choices of $\overline{\boldsymbol{R}}$. On the other hand, a constitutive relation can be formulated in a way that the response to a deformation incorporating any rigid body motion is obtained analytically from the response to the only

stretch part of that deformation. To this end, while generating the training and any testing datasets, we assume, without loss of generality, that the material experiences no rigid body rotation, i.e., $\overline{\boldsymbol{R}} = \mathbf{1}$, hence $\overline{\boldsymbol{F}} = e^{\bar{\varepsilon}}$ is a symmetric matrix.

For the rest of the paper, we omit the overbar symbol ($\bar{\square}$) of a macroscopic quantity, since the surrogate constitutive models rely only on macroscopic quantities.

3. Surrogate models

3.1. Structure of the neural networks

In this study, we propose two surrogate models for the macroscopic response of the porous elastomer, the architectures of which are schematically illustrated in Fig. 4. These are based on neural networks and use different macroscopic quantities as input and output features, as described in detail below (Sections 3.2–3). The training dataset was randomly split into 9:1 subsets used to train and validate, respectively. A test dataset was also generated, analysing the macroscopic response of the unit cell to random histories of multiaxial deformation (Section 3.4).

Prior to training of the NN, both input and output features of the learning dataset are normalised using a shifted min-max scaling function, which ensures that the zero-values in the actual dataset remain zero in the normalised dataset. The reason for this was that it is convenient to obtain a surrogate model which predicts vanishing stress when subject to vanishing strain. Accordingly, we construct the loss function to impart a high weight on training datapoints with strain close to zero. We propose a modified version of the mean absolute percentage error (mMAPE), i.e.

$$\text{mMAPE} = \sum_{i=1}^{n}\sum_{j=1}^{m} m\left(y_{i,j}\right)\cdot\left|y_{i,j}^{pred} - y_{i,j}\right| \tag{14}$$

$$m(y) = \begin{cases} -y^{-1} & y \le -y^{*} \\ ay + b & -y^{*} < y \le 0 \\ -ay + b & 0 < y \le y^{*} \\ y^{-1} & y > y^{*} \end{cases} \quad \text{if}$$

$$a = y^{*-2},\ b = ay^{*} + y^{*-1}$$

where y_i and y_i^{pred} denote the actual value and surrogate prediction of the i^{th} datapoint. mMAPE differs from MAPE in a region centred around y = 0 and bounded by $y = -y^*$ and $y = y^*$, attributing greater weight to datapoints in this region. The value $y^* = 0.02$ was chosen by trial and error in a preliminary study.

In order to preserve the rigid body modes, it is essential for a constitutive model to return a zero-stress response when subjected to zero-strain [46]. However, NNs do not naturally satisfy this vanishing stress condition since they inherently predict the response with a certain margin of error. In this study, we first aim to minimize the prediction error near zero input strain by employing the modified relative loss function mMAPE. Subsequently, we subtract the predicted output at zero input strain from the bias vector of the last layer of the NN. This linear correction ensures vanishing stress at vanishing strain, with a negligible impact on the overall predictive performance of the surrogate model. In the literature, various approaches have been proposed to address this issue [46,44,35].

To determine the hyperparameters of the model [57], we conduct a Bayesian optimisation. The hyperparameters to optimise are the number of hidden layers, the number of neurons per each hidden layer, which were assumed to be in the intervals [2,4] (hidden layers) and [10,500] (neurons per layer). For simplicity, we construct a NN with fixed number of neurons per each hidden layer and a single activation function for every neuron. Also, we leave to the optimiser the selection of the appropriate activation function between the *ReLU* (not applicable in Model 2, see discussion in Section 3.3) and *sigmoid* functions.

The optimisation and training of the NNs are carried out in TensorFlow 2.9. The optimisation of weight and biases of the NNs was performed by backpropagation using the Adam optimiser with an initial learning rate of 0.001 and a batch size of 64. The number of epochs was set to 1000 in each trial during the hyperparameter optimisation. An early-stopping criterion was also implemented (stop after 100 increments with no improvement to the loss). Detailed results of the hyperparameter optimisation study are presented in Appendix IV. After the hyperparameters were optimised, an additional training was performed in which the number of epochs was set to 10,000 (stop after 500 increments with no improvement to the loss).

3.2. Model 1: discovery of true stress

In Model 1, a multilayer feed forward NN, $\widehat{\boldsymbol{\sigma}}_{NN}(\boldsymbol{\varepsilon})$, is constructed for the discovery of the nonlinear relation between the true strain and true stress via direct regression. The optimum NN comprises of two hidden layers having 250 neurons each, where *ReLU* is the activation function. Therefore, the optimum NN of Model 1 can be expressed mathematically as:

$$\widehat{\boldsymbol{\sigma}}_{NN}\text{'} = \boldsymbol{W}_2\, f_{ReLU}\left(\boldsymbol{W}_1\, f_{ReLU}(\boldsymbol{W}_0\, \boldsymbol{\varepsilon}\text{'} + \boldsymbol{b}_0) + \boldsymbol{b}_1\right) + \boldsymbol{b}_2 \tag{15}$$

where $\widehat{\boldsymbol{\sigma}}_{NN'}$ and $\boldsymbol{\varepsilon}$' are the normalised non-dimensional output and input vectors, respectively, and $\boldsymbol{W}_l$ and $\boldsymbol{b}_l$ denote the weight matrix and bias vector of the l^{th} hidden layer, respectively.

We recall that the training dataset of $\widehat{\boldsymbol{\sigma}}_{NN}(\boldsymbol{\varepsilon})$ comprises of true stress responses to pure stretches only, i.e., no rigid body rotation. Accordingly, the input and output features of the NN are the 6 normalised non-dimensional components of the symmetric true strain and true stress tensors with any rigid body rotation neglected, respectively. However, a rigid body rotation is usually experienced by material points in finite element analyses of structures subjected to large deformations. Therefore, accurate prediction of the true stress can be made by considering any rigid body motion as:

$$\boldsymbol{\sigma} = \boldsymbol{R}\widehat{\boldsymbol{\sigma}}_{NN}(\boldsymbol{\varepsilon})\boldsymbol{R}^{\mathrm{T}}. \tag{16}$$

Eq. (16) suggests a constitutive model of the form $\boldsymbol{\sigma} = \boldsymbol{R}_{\mathscr{J}}(\boldsymbol{U})\boldsymbol{R}^{\mathrm{T}}$ which satisfies objectivity [58].

3.3. Model 2: discovery of a strain energy potential

Model 2 is a surrogate hyperelastic constitutive model as it consists of a NN, $\widehat{\mathscr{W}}_{NN}(\widetilde{I}_1,\widetilde{I}_2,J)$, which receives the first two invariants $(\widetilde{I}_1,\widetilde{I}_2)$ of the isochoric left Cauchy-Green deformation tensor $\widetilde{\boldsymbol{B}}$ and the volume ratio (J) as input and returns the corresponding non-dimensional strain energy density ($\mathscr{W}$) as output. The computation of the invariants from the user input true strain tensor and the computation of the true stress from the predicted strain energy density are performed on the basis of finite strain theory, as illustrated in Fig. 4.

For a prescribed true strain tensor $\boldsymbol{\varepsilon}$, the left and right Cauchy-Green deformation tensors $\boldsymbol{C}$ and $\boldsymbol{B}$, respectively, are obtained as:

$$\begin{aligned} \boldsymbol{C} &= e^{2\boldsymbol{\varepsilon}} \\ \boldsymbol{B} &= \boldsymbol{R}\boldsymbol{C}\boldsymbol{R}^{\mathrm{T}}. \end{aligned} \tag{17}$$

The invariants and the volume ratio, which are input to the NN, can be written in terms of $\boldsymbol{B}$ as:

$$\begin{aligned} \widetilde{I}_1 &= J^{-2/3}\mathrm{tr}(\boldsymbol{B}) \\ \widetilde{I}_2 &= \frac{1}{2J^{4/3}}\mathrm{tr}(\boldsymbol{B})^2 - \mathrm{tr}(\boldsymbol{B}^2) \\ J &= \sqrt{\det \boldsymbol{B}}. \end{aligned} \tag{18}$$

By selecting the input and output as the invariants of $\widetilde{\boldsymbol{B}}$ and strain energy density, the constitutive model satisfies material objectivity [51]. Furthermore, Model 2 assumes an isotropic material response,

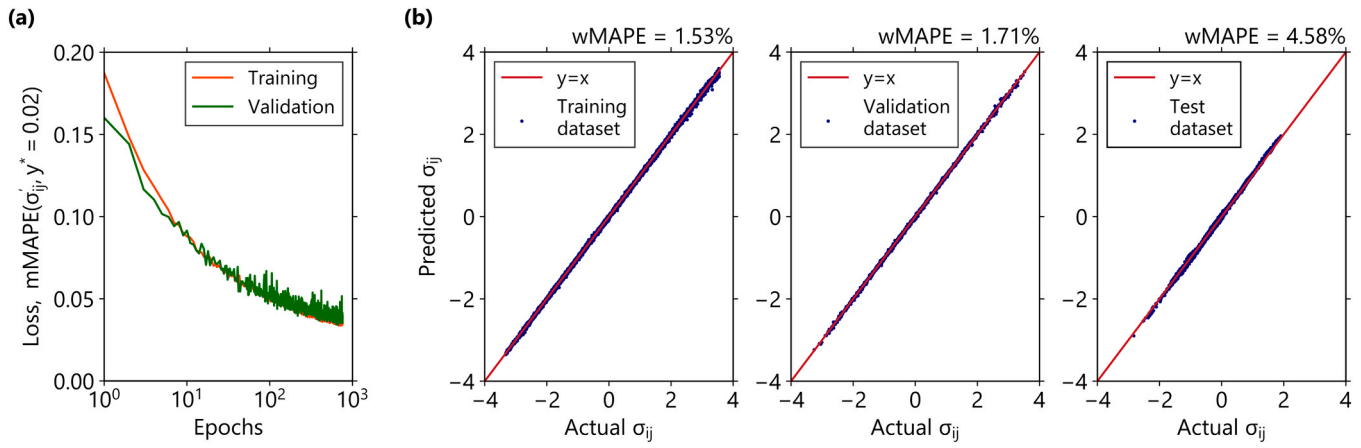


Fig. 5. (a) Summary of the NN learning procedure for Model 1 via training and validation loss curves, and (b) predictive performance of Model 1 over training, validation, and test datasets.

whereas Model 1 allows for capturing any slight anisotropy that could be exhibited by the material by employing full strain and stress tensors rather than their principal components.

The optimum NN structure for Model 2 consists of four hidden layers having 65 neurons each. As this surrogate model requires differentiation of the embedded NN with respect to its input features (see Eq. (4) or Eq. (21)), *ReLU* is not a suitable activation function for this model due to its discontinuous derivative. Accordingly, *sigmoid* is simply chosen as the activation function throughout $\widehat{\mathscr{W}}_{NN}(\widetilde{I}_1,\widetilde{I}_2,J)$. Therefore, the optimum NN of Model 2 can be expressed mathematically as:

$$\mathscr{W}' = \boldsymbol{W}_4 f_{sgmd}(\boldsymbol{W}_3 f_{sgmd}(\boldsymbol{W}_2 f_{sgmd}(\boldsymbol{W}_1 f_{sgmd}(\boldsymbol{W}_0 \widetilde{I}' + \boldsymbol{b}_0) + \boldsymbol{b}_1) + \boldsymbol{b}_2) + \boldsymbol{b}_3) + \boldsymbol{b}_4 \tag{19}$$

where $\mathscr{W}'$ is the scalar output (normalised strain energy density) and $\widetilde{\boldsymbol{I}}$ is the vector input (consisting of normalised invariants) of $\widehat{\mathscr{W}}_{NN}(\widetilde{I}_1,\widetilde{I}_2,J)$, respectively. Following the prediction of strain energy density $\mathscr{W}$, the true stress tensor can be computed by:

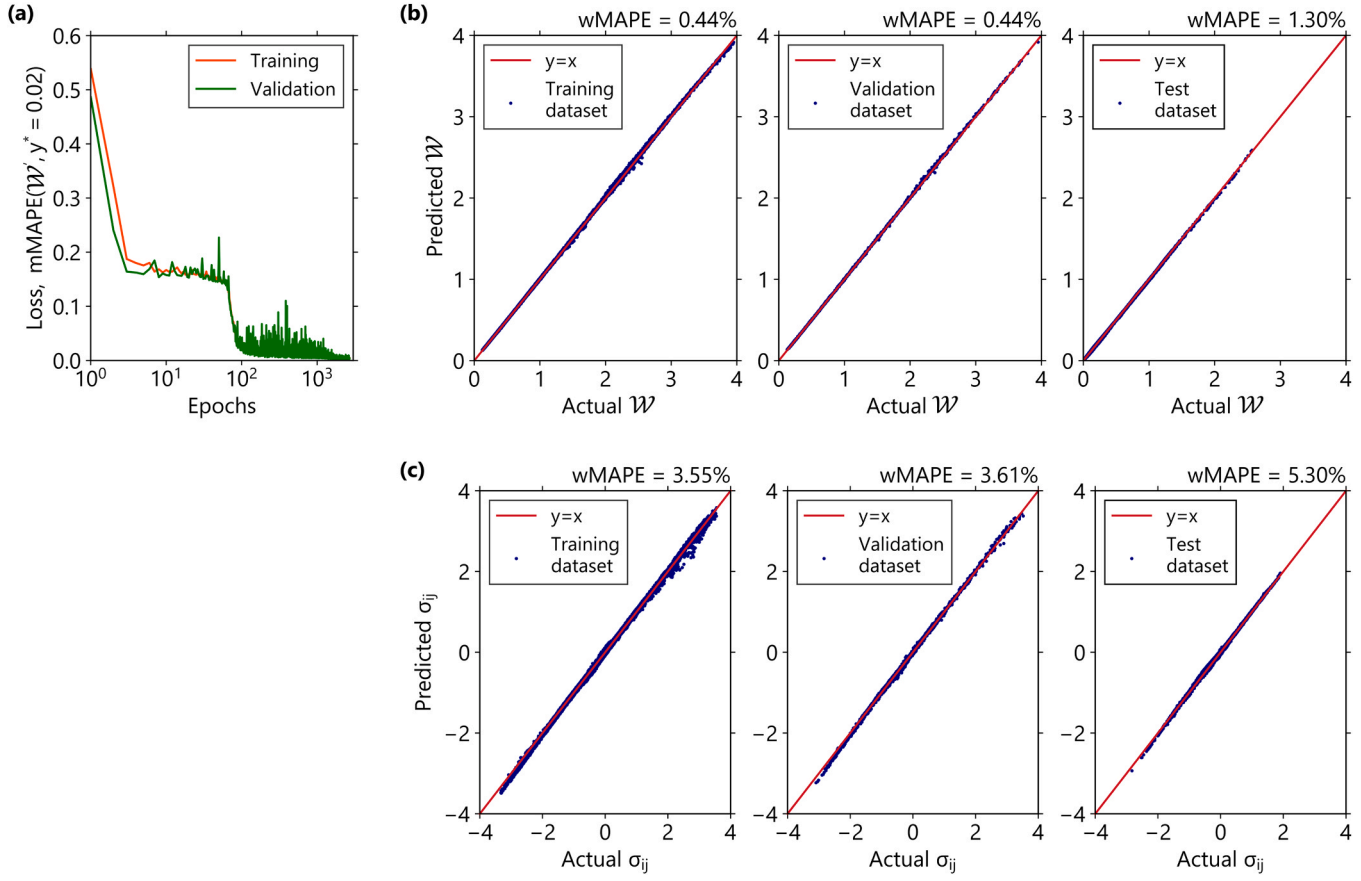


Fig. 6. (a) Summary of the NN learning procedure for Model 2 via training and validation loss curves, and performance of Model 2 in predicting (b) $\mathscr{W}$ and (c) σ over training, validation, and test datasets.

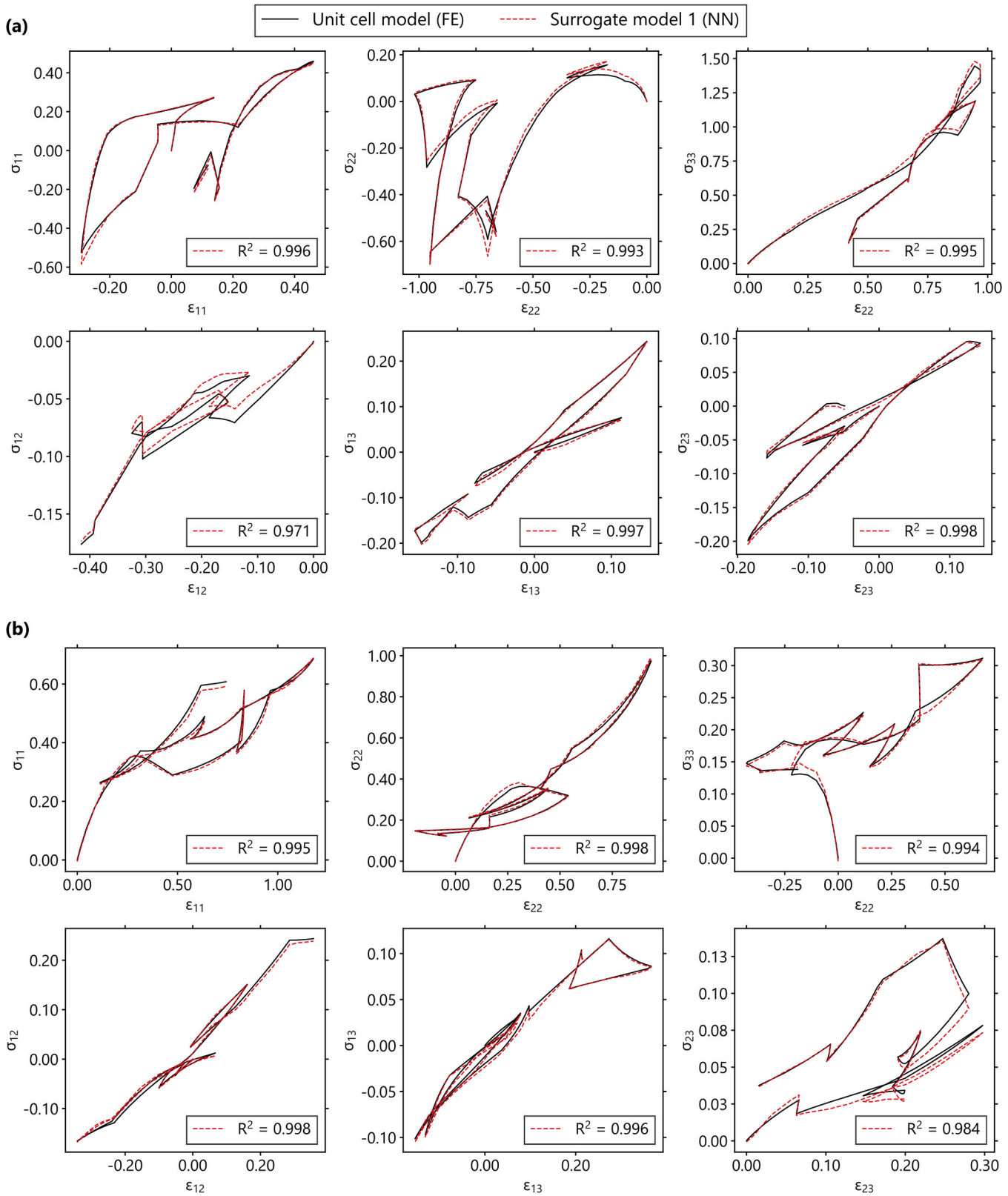


Fig. 7. Stress-strain histories for the porous unit cell from two FE test simulations (a-b). Predictions of Model 1 are compared to the FE predictions. The R^2 values are also indicated in every graph.

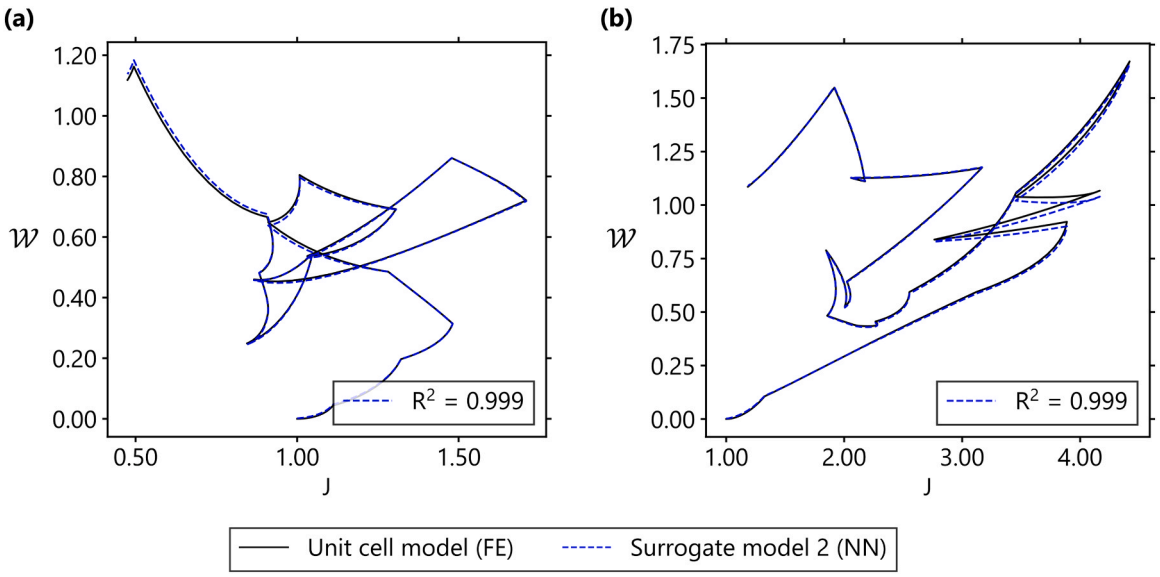


Fig. 8. Strain energy density vs macroscopic volume ratio histories for the porous unit cell loaded by two different random strain histories (a-b). The strain energy density predictions of Model 2 are compared to the FE predictions.

$$\sigma = \frac{2}{J}\left[\frac{1}{J^{2/3}}\left(\frac{\partial \mathscr{W}}{\partial \widetilde{I}_1} + \widetilde{I}_1\frac{\partial \mathscr{W}}{\partial \widetilde{I}_2}\right)\boldsymbol{B} - \frac{1}{J^{4/3}}\frac{\partial \mathscr{W}}{\partial \widetilde{I}_2}\boldsymbol{B}\cdot\boldsymbol{B}\right] + \left[\frac{\partial \mathscr{W}}{\partial J} - \frac{2}{3J}\left(\widetilde{I}_1\frac{\partial \mathscr{W}}{\partial \widetilde{I}_1} + 2\widetilde{I}_2\frac{\partial \mathscr{W}}{\partial \widetilde{I}_2}\right)\right]\mathbf{1} \tag{20}$$

where $\partial \mathscr{W}/\partial \widetilde{I}_1$, $\partial \mathscr{W}/\partial \widetilde{I}_2$, and $\partial \mathscr{W}/\partial J$ are partial derivatives that must be taken either analytically using Eq. (19) or numerically by using the symmetric approximation of partial derivative as:

$$\frac{\partial \mathscr{W}}{\partial \widetilde{I}_i} \approx \frac{\mathscr{W}(\widetilde{I}_i + \Delta\widetilde{I}_i) - \mathscr{W}(\widetilde{I}_i - \Delta\widetilde{I}_i)}{2\Delta\widetilde{I}_i} \tag{21}$$

where $\widetilde{I}_i$ denotes any of the invariants $\widetilde{I}_1, \widetilde{I}_2$, and J. $\Delta\widetilde{I}_i$ is the increment in $\widetilde{I}_i$ and has to be chosen as small as possible.

The analytical computation of partial derivatives of the strain energy is straightforward from a mathematical perspective, yet it proves to be computationally inefficient due to the requirement of numerous matrix operations for each strain point. On the other hand, the numerical calculation of $\partial \mathscr{W}/\partial \widetilde{I}_i$ comes at a negligible computational cost; however, the accuracy of the calculated value is highly dependent on the selection of $\Delta\widetilde{I}_i$. In this study, we opt for numerical differentiation as defined in Eq. (22). To achieve the closest approximation to the analytical computation, we determine the value of $\Delta\widetilde{I}_i$ through a trial-and-error process.

3.4. Measuring model performance

To evaluate the performance of the surrogate constitutive models, we generate an unseen set of data, which is the assembly of datapoints collected from 80 multiaxial test simulations. In each multiaxial test simulation, we impose a pseudo-random macroscopic true strain history to the porous unit cell and measure its homogenised mechanical response. The pseudo-random histories trace a path of random segments in the 6-D true strain space until meeting the termination condition $\|\boldsymbol{\varepsilon}\|_F \geq 2$ or reaching a total of 20 segments. The magnitude of random relative change in a component of the true strain tensor along a single segment is controlled by:

$$\Delta\varepsilon_{ij} = \mathrm{sgn}(r_{\beta,ij} - \theta)\left[\Delta\varepsilon_{\min} + r_{\alpha,ij}(\Delta\varepsilon_{\max} - \Delta\varepsilon_{\min})\right] \tag{22}$$

where $\Delta\varepsilon_{\min} = 0.001$ and $\Delta\varepsilon_{\max} = 0.2$ are the extreme values of the relative change of a strain component per segment. $r_{\beta,ij}$ and $r_{\alpha,ij}$ are random numbers generated from the uniform distribution on the interval [0,1], and $\theta = 0.5$ ensures the equal probability of negative and positive relative strain changes in every segment. All FE simulations were performed following the methodology described in 2.2.

To measure the accuracy of the predictions by the surrogate models, we use the weighted mean absolute percentage error (wMAPE) where the absolute percentage error of each of m output features along n data rows are weighted by their actual values as:

$$\mathrm{wMAPE} := \frac{\sum_{i=1}^{n}\sum_{j=1}^{m}\left(y_{i,j}\cdot\frac{\left|y_{i,j}^{pred} - y_{i,j}\right|}{\left|y_{i,j}\right|}\right)}{\sum_{i=1}^{n}\sum_{j=1}^{m} y_{i,j}} = \frac{\sum_{i=1}^{n}\sum_{j=1}^{m}\left|y_{i,j}^{pred} - y_{i,j}\right|}{\sum_{i=1}^{n}\sum_{j=1}^{m}\left|y_{i,j}\right|}. \tag{23}$$

A summary of the performance evaluation of the Model 1 is presented in Fig. 5 by means of the training and validation loss curves (a), and prediction accuracies of the training, validation, and test datasets (b). Fig. 5b shows low deviations of the predictions from the line of best fit (y=x), with wMAPE well below 5%, suggesting a high predictive accuracy of the NN.

Similarly, a summary of the performance evaluation of the Model 2 is presented in Fig. 6 by means of the training and validation loss curves (a), and prediction accuracies of the training, validation, and test datasets specifically for strain energy density (b) and true stress (c). Fig. 6b shows low deviations of strain energy density predictions from the line of best fit (y=x), with wMAPE well below 1.5%, suggesting a high predictive accuracy of the NN. However, deviations of true stress predictions of Model 2 from the line of best fit are considerably higher than its predictions of the strain energy density, as a consequence of error amplification in the differentiation process.

The observation that the test error is considerably larger than the training and validation errors in both surrogate models does not necessarily indicate an overfitting problem. This discrepancy is, in fact, an expected outcome of the application of different sampling techniques. The training and validation datasets consist of data generated at true strain states uniformly spanning $\mathbb{R}^6$. However, the test dataset is a compilation of data series extracted from numerous multiaxial test simulations, each starting from an undeformed state and following

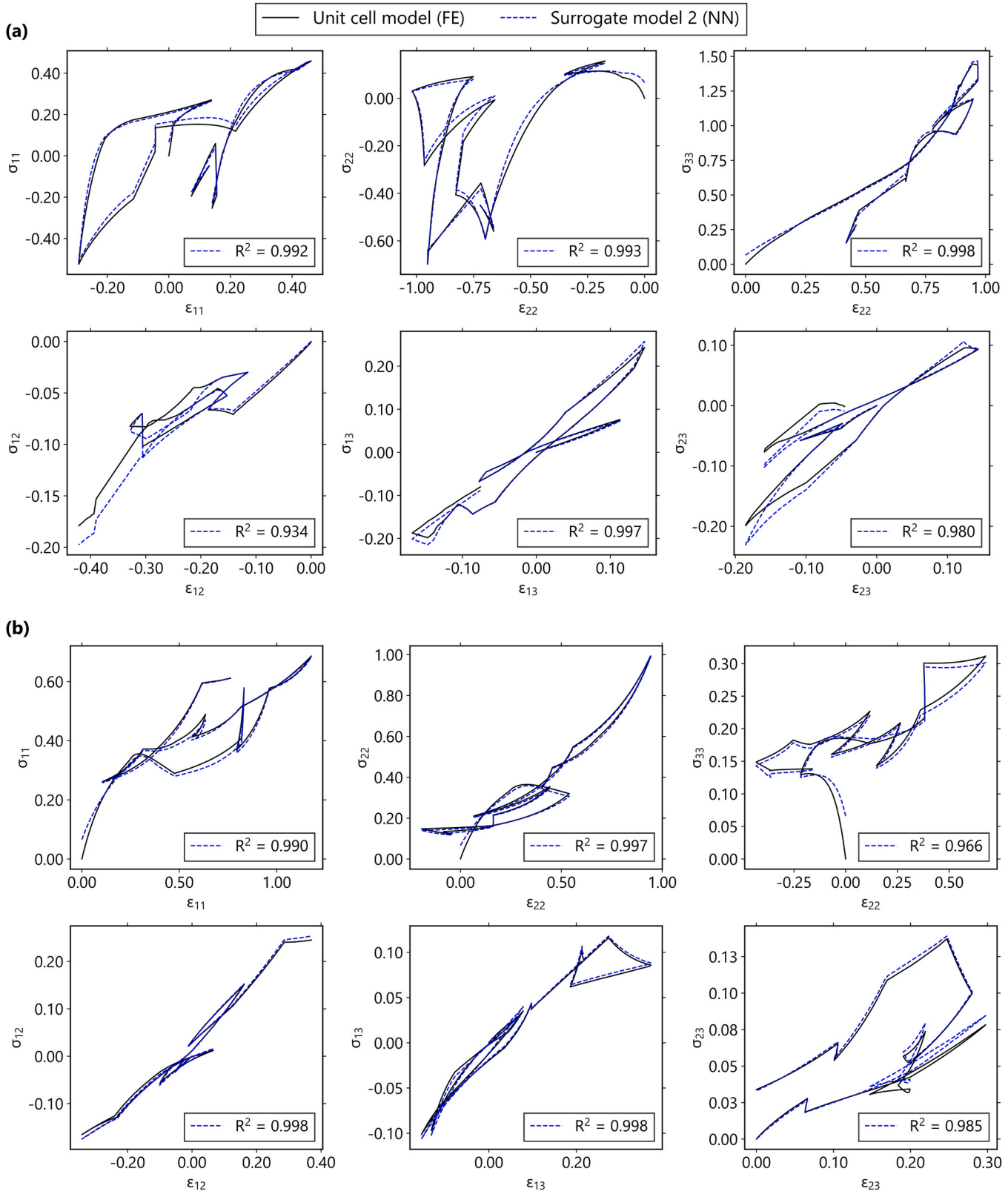


Fig. 9. Stress-strain histories for the porous unit cell from two FE test simulations (a-b). True stress predictions of the Model 2 are compared to the FE predictions by means of R^2 values.

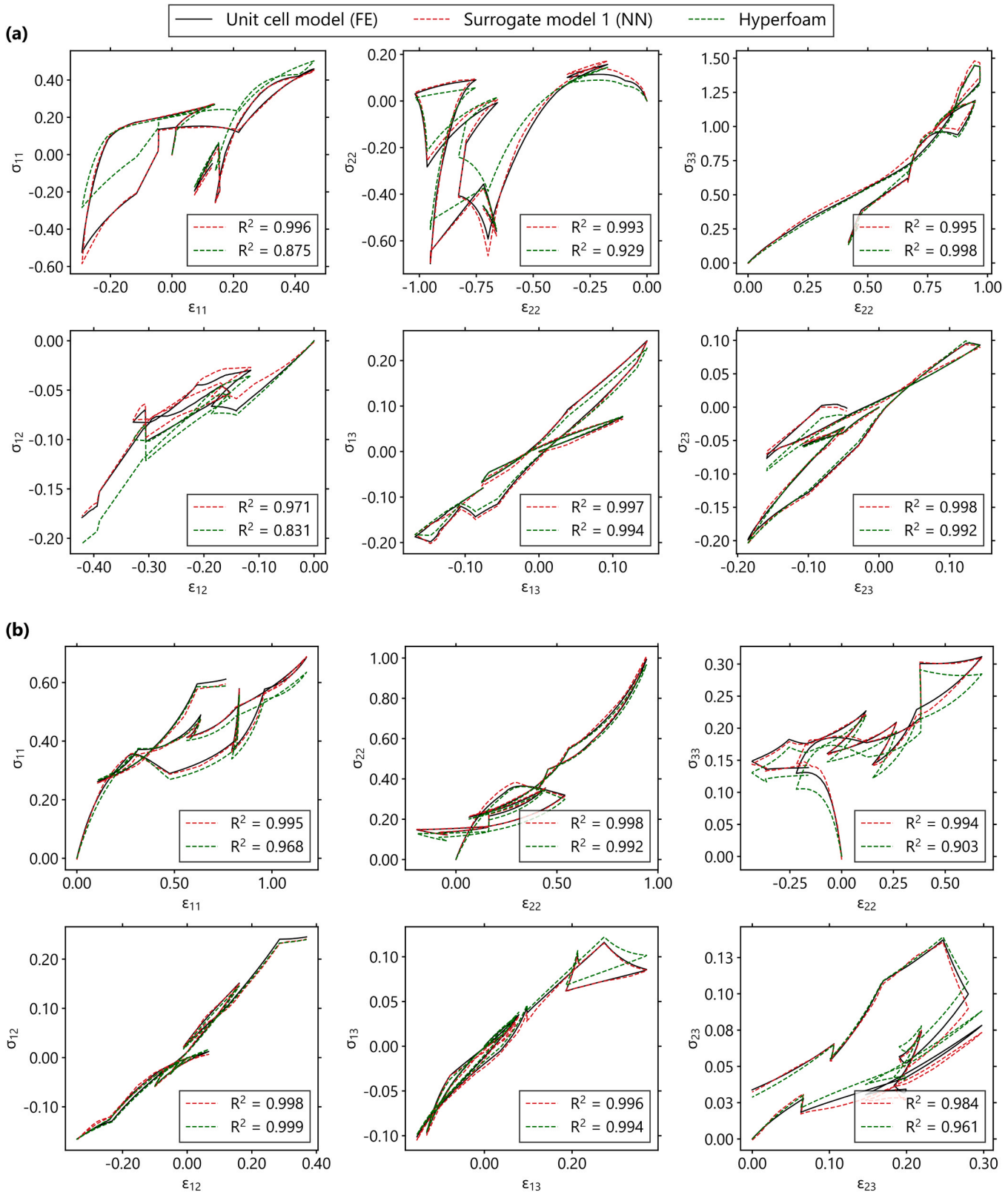


Fig. 10. Selected stress-strain histories for the porous unit cell in two different FE test simulations (a-b). True stress predictions of Model 1 are compared to the Hyperfoam model and to FE predictions of the response of a unit cell.

random true strain paths in $\mathbb{R}^6$. Therefore, the data frequency in the test dataset around the zero-strain/stress region is relatively higher, leading to a larger overall relative error than what we would anticipate with a uniform distribution.

4. Results and discussion

4.1. Predictions of Model 1

To better illustrate the predictive ability of Model 1, in Fig. 7 we present two example test cases with relatively large number of steps. The surrogate model provides excellent predictions of the stress versus strain histories, with very high coefficients of determination (R^2-scores).

4.2. Predictions of Model 2

Model 2 establishes a stress-strain relation via a NN which predicts the strain energy density $\mathscr{W}$ as a function of three invariants $\widetilde{I}_1, \widetilde{I}_2$, and J. The predictions of the $\mathscr{W}$ - J histories in two test cases are presented in Fig. 8 and compared with the FE predictions. $R^2 = 0.999$ quantifies the excellent agreement between the predictions of $\mathscr{W}$ by the NN and the FE simulations.

In Fig. 9 the true stress vs true strain predictions of Model 2 are compared to the predictions of the unit cell model, for two selected random strain histories. A good accuracy is demonstrated, however marginally lower than that of Model 1. Moreover, true stress predictions of Model 2 have considerably lower accuracy than its predictions of the strain energy density, as a consequence of error amplification in the differentiation process.

4.3. Comparison to Hyperfoam model

We chose the optimised Model 1, of higher accuracy, to compare its predictive ability to that of the widely known Hyperfoam model (also called as Storakers foam model, Ogden foam model, and Hill foam model by various commercial FE software packages). Hyperfoam is an Ogden type phenomenological hyperelastic constitutive model governed by a principal stretch-based strain energy density function [18] as defined by:

$$\mathscr{W} = \sum_{i=1}^{p} \frac{2\mu_i}{\alpha_i^2}\left[\lambda_1^{\alpha_i} + \lambda_2^{\alpha_i} + \lambda_3^{\alpha_i} - 3 + \frac{1}{\beta_i}\left(J^{-\alpha_i\beta_i} - 1\right)\right] \tag{24}$$

where λ_k ($k = 1, 2, 3$) are principal stretches, μ_i, α_i, and β_i are material parameters, and p is the strain energy potential order. Hyperfoam differs from traditional hyperelastic constitutive models in predicting a Poisson's ratio independent from the imposed strain. This makes Hyperfoam a specialised model that is suitable for modelling the large strain mechanical response of elastomeric foams.

The material parameters required by the Hyperfoam model were determined by fitting the stress expressions that can be derived from Eq. (25) to the stress-strain data obtained from simple experiments on the elastomeric unit cell. More specifically, from the uniaxial, equibiaxial, simple shear, planar, and volumetric test data. In this study we conducted virtual uniaxial, equibiaxial, planar, and simple shear tests, as recommended by ABAQUS, and the software conducted an automatic regression to determine the material's parameters for Hyperfoam. Further details of the material parameter characterisation for the Hyperfoam model can be found in Appendix V.

The predictive capabilities of the best surrogate model and the Hyperfoam model are compared by assessing their agreement with the unit cell model in predicting the true stress vs true strain histories recorded in the two example test cases, as presented in Fig. 10. Although Hyperfoam predicts a shear response similar to the unit cell model ($R^2 > 0.96$), a similar agreement is not achieved in the case of normal stresses as suggested by considerably low R^2 values. On the other hand, as noted in 4.1, the surrogate model is in excellent agreement with the unit cell model. Compared to Hyperfoam, the surrogate model demonstrates higher accuracy in predicting the true stress – true strain behaviour of a porous unit cell.

5. Concluding remarks

We used data from the FE analysis of the response of the unit cell of a porous elastomer to train two different data-driven models. Model 1 predicted true stress as a function of true strain, while Model 2 predicted the strain energy density as a function of the strain invariants. Model 1 exhibited slightly higher accuracy and simpler application compared to Model 2. Nevertheless, both models demonstrated excellent predictive capabilities in complex multiaxial loading, with Model 1 outperforming an established phenomenological model for porous elastomers.

Both models maintain the fidelity to the underlying physics of the problem by accurately reproducing the stress response of a high-fidelity unit cell finite element model under arbitrary loading, satisfying approximately all the laws of mechanics that the material must obey [59,60] as well as the objectivity condition.

CRediT authorship contribution statement

Vito L Tagarielli: Writing – review & editing, Supervision, Resources, Project administration, Conceptualization. **Mirac Onur Bozkurt:** Writing – original draft, Visualization, Software, Methodology, Investigation, Formal analysis, Data curation.

Declaration of Competing Interest

The authors declare that they have no known competing financial interests or personal relationships that could have appeared to influence the work reported in this paper.

Data availability

Data will be made available on request.

Acknowledgements

We acknowledge funding from the Ministry of National Education of the Republic of Turkey, supporting the Ph.D. research of M. Onur Bozkurt.

Appendix A. Supporting information

Supplementary data associated with this article can be found in the online version at doi:10.1016/j.eml.2024.102170.

References

[1] A.K. Bastola, L. Li, A new type of vibration isolator based on magnetorheological elastomer, Mater. Des. 157 (2018) 431–436.
[2] A. Dourbash, C. Buratti, E. Belloni, S. Motahari, Preparation and characterization of polyurethane/silica aerogel nanocomposite materials, J. Appl. Polym. Sci. 134 (2017).
[3] A. Fraleoni-Morgera, M. Chhikara, Polymer-based nano-composites for thermal insulation, Adv. Eng. Mater. 21 (2019) 1801162.
[4] R. Adams, S. Townsend, S. Soe, P. Theobald, Finite element-based optimisation of an elastomeric honeycomb for impact mitigation in helmet liners, Int J. Mech. Sci. 214 (2022) 106920.
[5] E.C. Clough, T.A. Plaisted, Z.C. Eckel, K. Cante, J.M. Hundley, T.A. Schaedler, Elastomeric microlattice impact attenuators, Matter 1 (2019) 1519–1531.
[6] B. Amsden, Curable, biodegradable elastomers: emerging biomaterials for drug delivery and tissue engineering, Soft Matter 3 (2007) 1335–1348.
[7] B.G. Amsden, Biodegradable elastomers in drug delivery, Expert Opin. Drug Deliv. 5 (2008) 175–187.
[8] X.L. Zhang, C.L. Jia, X.Y. Qiao, T.Y. Liu, K. Sun, Porous poly(glycerol sebacate) (PGS) elastomer scaffolds for skin tissue engineering, Polym. Test. 54 (2016) 118–125.

[9] J. Ham, T.M. Huh, J. Kim, J.-O. Kim, S. Park, M.R. Cutkosky, Z. Bao, Porous Dielectric Elastomer Based Flexible Multiaxial Tactile Sensor for Dexterous Robotic or Prosthetic Hands, Adv. Mater. Technol. 8 (2023) 2200903.
[10] K. Park, S. Kim, H. Lee, I. Park, J. Kim, Low-hysteresis and low-interference soft tactile sensor using a conductive coated porous elastomer and a structure for interference reduction, Sens. Actuators a Phys. 295 (2019) 541–550.
[11] S. Jung, J.H. Kim, J. Kim, S. Choi, J. Lee, I. Park, T. Hyeon, D.H. Kim, Reverse-micelle-induced porous pressure-sensitive rubber for wearable human-machine interfaces, Adv. Mater. 26 (2014) 4825–4830.
[12] Y.J. Fan, X.S. Meng, H.Y. Li, S.Y. Kuang, L. Zhang, Y. Wu, Z.L. Wang, G. Zhu, Stretchable porous carbon nanotube-elastomer hybrid nanocomposite for harvesting mechanical energy, Adv. Mater. 29 (2017).
[13] R.W. Ogden, Extremum principles in non-linear elasticity and their application to composites—I: theory, Int. J. Solids Struct. 14 (1978) 265–282.
[14] Z. Hashin, Large isotropic elastic deformation of composites and porous media, Int J. Solids Struct. 21 (1985) 711–720.
[15] M. Danielsson, D.M. Parks, M.C. Boyce, Constitutive modeling of porous hyperelastic materials, Mech. Mater. 36 (2004) 347–358.
[16] B. Shrimali, V. Lefevre, O. Lopez-Pamies, A simple explicit homogenization solution for the macroscopic elastic response of isotropic porous elastomers, J. Mech. Phys. Solids 122 (2019) 364–380.
[17] A.K. Landauer, X.Q. Li, C. Franck, D.L. Henann, Experimental characterization and hyperelastic constitutive modeling of open-cell elastomeric foams, J. Mech. Phys. Solids 133 (2019).
[18] B. Storåkers, On material representation and constitutive branching in finite compressible elasticity, J. Mech. Phys. Solids 34 (1986) 125–145.
[19] S. Saeb, P. Steinmann, A. Javili, Aspects of computational homogenization at finite deformations: a unifying review from Reuss' to Voigt's bound, Appl. Mech. Rev. 68 (2016).
[20] J. Yvonnet, D. Gonzalez, Q.C. He, Numerically explicit potentials for the homogenization of nonlinear elastic heterogeneous materials, Comput. Method Appl. M 198 (2009) 2723–2737.
[21] J. Yvonnet, E. Monteiro, Q.-C. He, Computational homogenization method and reduced database model for hyperelastic heterogeneous structures 11 (2013) 201–225.
[22] J. Moraleda, J. Segurado, J. Llorca, Finite deformation of porous elastomers: a computational micromechanics approach, Philos. Mag. 87 (2007) 5607–5627.
[23] J. Yvonnet, Q.C. He, The reduced model multiscale method (R3M) for the non-linear homogenization of hyperelastic media at finite strains, J. Comput. Phys. 223 (2007) 341–368.
[24] Y. Wang, D.L. Henann, Finite-element modeling of soft solids with liquid inclusions, Extrem. Mech. Lett. 9 (2016) 147–157.
[25] Y. Chen, W.T. Guo, P.P. Yang, J.H. Zhao, Z.Y. Guo, L.T. Dong, Z. Zhong, Constitutive modeling of neo-Hookean materials with spherical voids in finite deformation, Extrem. Mech. Lett. 24 (2018) 47–57.
[26] Z.Y. Guo, Y. Chen, X.Q. Peng, X.H. Shi, H.T. Li, Y.L. Chen, Shear stiffness of neo-Hookean materials with spherical voids, Compos Struct. 150 (2016) 21–27.
[27] P. Yang, Z. Guo, N. Hu, W. Sun, Y. Chen, Hyperelastic behaviors of closed-cell porous materials at a wide porosity range, Compos Struct. 294 (2022) 115792.
[28] B.A. Le, J. Yvonnet, Q.C. He, Computational homogenization of nonlinear elastic materials using neural networks, Int. J. Numer. Methods Eng. 104 (2015) 1061–1084.
[29] M.A. Bessa, R. Bostanabad, Z. Liu, A. Hu, D.W. Apley, C. Brinson, W. Chen, W. K. Liu, A framework for data-driven analysis of materials under uncertainty: countering the curse of dimensionality, Comput. Method Appl. M 320 (2017) 633–667.
[30] M. Mozaffar, R. Bostanabad, W. Chen, K. Ehmann, J. Cao, M.A. Bessa, Deep learning predicts path-dependent plasticity, Proc. Natl. Acad. Sci. USA (2019).
[31] C. Yang, Y. Kim, S. Ryu, G.X. Gu, Prediction of composite microstructure stress-strain curves using convolutional neural networks, Mater. Des. 189 (2020) 108509.
[32] W. Ge, V.L. Tagarielli, A computational framework to establish data-driven constitutive models for time- or path-dependent heterogeneous solids, Sci. Rep. 11 (2021) 15916.
[33] W. Ge, V.L. Tagarielli, Data-driven homogenisation of the response of heterogeneous ductile solids with isotropic damage, Mater. Des. 238 (2024) 112738.
[34] H.J. Logarzo, G. Capuano, J.J. Rimoli, Smart constitutive laws: inelastic homogenization through machine learning, Comput. Method Appl. M 373 (2021) 113482.
[35] A. Frankel, C.M. Hamel, D. Bolintineanu, K. Long, S. Kramer, Machine learning constitutive models of elastomeric foams, Comput. Method Appl. M 391 (2022) 114492.
[36] B. Tasdemir, A. Pellegrino, V. Tagarielli, A strategy to formulate data-driven constitutive models from random multiaxial experiments, Sci. Rep. 12 (2022) 22248.
[37] B. Tasdemir, V. Tagarielli, A. Pellegrino, A data-driven model of the yield and strain hardening response of commercially pure titanium in uniaxial stress, Mater. Des. 229 (2023) 111878.
[38] E. Salvati, A. Tognan, L. Laurenti, M. Pelegatti, F. De Bona, A defect-based physics-informed machine learning framework for fatigue finite life prediction in additive manufacturing, Mater. Des. 222 (2022) 111089.
[39] A. Tognan, E. Salvati, Probabilistic defect-based modelling of fatigue strength for incomplete datasets assisted by literature data, Int. J. Fatigue 173 (2023) 107665.
[40] C.M. Hamel, K.N. Long, S.L.B. Kramer, Calibrating constitutive models with full-field data via physics informed neural networks, Strain 59 (2023) e12431.
[41] K. Guo, Z. Yang, C.-H. Yu, M.J. Buehler, Artificial intelligence and machine learning in design of mechanical materials, Mater. Horiz. 8 (2021) 1153–1172.
[42] J. Ling, R. Jones, J. Templeton, Machine learning strategies for systems with invariance properties, J. Comput. Phys. 318 (2016) 22–35.
[43] N.N. Vlassis, R. Ma, W. Sun, Geometric deep learning for computational mechanics Part I: anisotropic hyperelasticity, Comput. Method Appl. M 371 (2020) 113299.
[44] M. Fernández, M. Jamshidian, T. Böhlke, K. Kersting, O. Weeger, Anisotropic hyperelastic constitutive models for finite deformations combining material theory and data-driven approaches with application to cubic lattice metamaterials, Comput. Mech. 67 (2021) 653–677.
[45] K. Linka, M. Hillgärtner, K.P. Abdolazizi, R.C. Aydin, M. Itskov, C.J. Cyron, Constitutive artificial neural networks: a fast and general approach to predictive data-driven constitutive modeling by deep learning, J. Comput. Phys. 429 (2021) 110010.
[46] F. As'ad, P. Avery, C. Farhat, A mechanics-informed artificial neural network approach in data-driven constitutive modeling, Int J. Numer. Meth Eng. 123 (2022), 2738-2759.
[47] J.N. Fuhg, G.A. Padmanabha, N. Bouklas, B. Bahmani, W. Sun, N.N. Vlassis, M. Flaschel, P. Carrara, L. De Lorenzis, A Review on Data-driven Constitutive Laws for Solids (2024) arXiv preprint arXiv:2405.03658.
[48] D.K. Lin, T.W. Simpson, W. Chen, Sampling strategies for computer experiments: design and analysis, Int. J. Reliab. Appl. 2 (2001) 209–240.
[49] R. Harman, V. Lacko, On decompositional algorithms for uniform sampling from n-spheres and n-balls, J. Multivar. Anal. 101 (2010) 2297–2304.
[50] R.W. Rice, Limitations of pore-stress concentrations on the mechanical properties of porous materials, J. Mater. Sci. 32 (1997) 4731–4736.
[51] A.F. Bower, Applied Mechanics of Solids, CRC Press, 2009.
[52] E.V. González, P. Maimí, A. Turon, P.P. Camanho, J. Renart, Simulation of delamination by means of cohesive elements using an explicit finite element code. Computers, Mater. \ Contin. (2009) 9.
[53] D.M. Kochmann, LLecture Notes on Multiscale Modeling (2022).
[54] M.G.D. Geers, V.G. Kouznetsova, W.A.M. Brekelmans, Multi-scale computational homogenization: trends and challenges, J. Comput. Appl. Math. 234 (2010) 2175–2182.
[55] W. Tian, L. Qi, X. Chao, J. Liang, M. Fu, Periodic boundary condition and its numerical implementation algorithm for the evaluation of effective mechanical properties of the composites with complicated micro-structures, Compos. Part B Eng. 162 (2019) 1–10.
[56] D. Garoz, F.A. Gilabert, R.D.B. Sevenois, S.W.F. Spronk, W. Van Paepegem, Consistent application of periodic boundary conditions in implicit and explicit finite element simulations of damage in composites, Compos. Part B Eng. 168 (2019) 254–266.
[57] Y. Bengio, Practical recommendations for gradient-based training of deep architectures, in: Neural Networks: Tricks of the Trade, Springer, 2012, pp. 437–478.
[58] L.E. Malvern, IIntroduction to the Mechanics of A Continuous Medium. (1969).
[59] J. Ghaboussi, J.H. Garrett, X. Wu, Knowledge-based modeling of material behavior with neural networks, J. Eng. Mech. 117 (1991) 132–153.
[60] Y. Yamanaka, S. Matsubara, N. Hirayama, S. Moriguchi, K. Terada, Surrogate modeling for the homogenization of elastoplastic composites based on RBF interpolation, Comput. Method Appl. M 415 (2023) 116282.